ACS OMEGA

Open Access

This article is licensed under CC-BY-NC-ND 4.0

http://pubs.acs.org/journal/acsodf

Article

Fe_3O_4/CuO/Chitosan Nanocomposites: An Ultrasound-Assisted Green Approach for Antibacterial and Photocatalytic Properties

Published as part of ACS Omega virtual special issue "Magnetic Nanohybrids for Environmental Applications".

Nguyen Thi Huong,* Pham Thi Mai Huong, Nguyen Thi Kim Giang, Phung Thi Lan, Vu Thanh Dong, and Cong Tien Dung

Cite This: *ACS Omega* 2023, 8, 42429−42439

Read Online

ACCESS | Metrics & More | Article Recommendations

ABSTRACT: The fundamental goal of this research was to use an environmentally friendly sonochemical method to synthesize a Fe_3O_4/CuO/chitosan magnetic nanocomposite. The nanocomposites featured particle sizes ranging from 50 to 90 nm, and structural characteristics were thoroughly examined. Moreover, the material displayed selective photodegradation capabilities with MB, achieving an impressive efficiency of nearly 98% within 180 min under specific conditions. Notably, the material's reusability was remarkable, maintaining an efficiency of approximately 88% even after five cycles. The possible photodegradation mechanism was proposed based on the evaluation of energy bands, along with a comprehensive analysis of the impacts on MB photodegradation. Concurrently, adsorption isotherms and kinetic models were evaluated. Additionally, this material exhibited promising antibacterial activity against *Saccharomyces cerevisiae*, *Bacillus subtilis*, and *Escherichia coli*. These findings suggested that the Fe_3O_4/CuO/chitosan material could be utilized in real-world scenarios for environmental purification due to its ability to function as a photocatalyst and antibacterial agent.

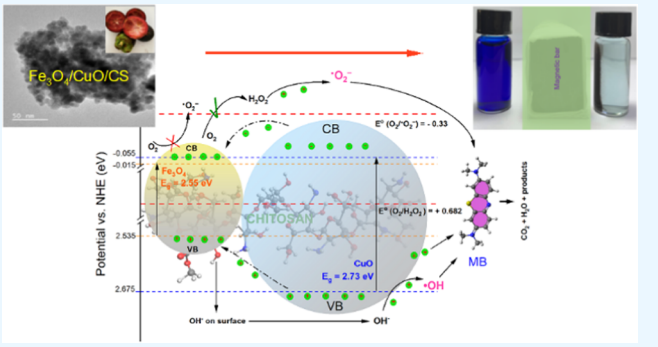

1. INTRODUCTION

Over the past few years, various techniques have been developed and employed to investigate and synthesize metal oxide materials. Owing to their special physicochemical properties, such as different thermal, optical, electrical, and mechanical features, these materials have been used in many fields, including environmental treatment,[1−3] antibacterial systems,[4−6] magnetic sensors,[7] electrochemical batteries,[8] and fuel cells.[9] In addition to coprecipitation,[10] hydrothermal,[11] sol-gel,[11] and plasma[12] methods, which are currently being developed, green synthesis methods use extracts from leaves, fruit peel,[13] bacteria,[14] and vitamins.[15] Moreover, some fungi containing active redox species have been tested as reagents and stabilizers. In this work, we have successfully synthesized Fe_3O_4/CuO/chitosan (CS) nanocomposites using a coprecipitation-based and ultrasound-assisted green method. However, in order to limit the agglomeration of Fe_3O_4 and CuO nanoparticles (NPs) in this system and increase their recovery rate when applied as environmental treatment materials, we used the chitosan biopolymer as a dispersant.

CS is a polyaminosaccharide with disinfectant properties and the ability to adsorb heavy metals, immobilize enzymes, and deliver drugs; it also exhibits good biocompatibility.[16] Therefore, modifying Fe_3O_4/CuO nanosystems with chitosan can yield promising materials with many significant applications in medicine and environmental science.

Wu et al. synthesized a Fe_3O_4-chitosan/sodium tripolyphosphate (TPP) system by coprecipitation in an alkaline solution in an inert (N_2) environment at 60 °C for 2 h. The formation of cross-links between chitosan and TPP with the ferromagnetic Fe_3O_4 nucleus produced the micropore system of the CS gel. The final product had a high saturation magnetization at 60 °C, which was considered the optimal temperature for both CS and TPP cross-linking and $Fe(OH)_2$ oxidation; this is because this temperature was high enough to form cross-links, but not for the oxidation of Fe^{2+} to Fe^{3+}, which would result in the material losing its magnetic properties. The Fe_3O_4-CS/TPP system could immobilize lipase enzymes without inactivating them.[17] Chang et al. synthesized chitosan-Fe_3O_4 by a hydrothermal method at 80 °C and applied it to adsorb

Received: July 11, 2023
Revised: October 20, 2023
Accepted: October 20, 2023
Published: November 3, 2023

Downloaded via 1.54.208.57 on December 17, 2024 at 18:27:18 (UTC).
See https://pubs.acs.org/sharingguidelines for options on how to legitimately share published articles.

ACS Publications

© 2023 The Authors. Published by American Chemical Society

https://doi.org/10.1021/acsomega.3c04956
ACS Omega 2023, 8, 42429−42439

Cu^{2+} ions in water, reaching a maximum adsorption capacity of 21.5 mg/g. In particular, CS increased the specific surface area and changed the isoelectric point, thereby accelerating the Cu^{2+} adsorption process.[18] Therefore, the use of CS in nanocomposite systems has attracted significant interest in recent years, owing to its ability to act as a cross-linking agent to help disperse metal oxides, alter the surface charge of the material, and facilitate recovery thanks to the external magnetic field of iron oxide NPs.[18,19]

Furthermore, in previous studies, materials based on Fe_3O_4,[20] CuO,[21] and CS[22] have been examined to inhibit the growth of various microorganisms, including *Staphylococcus aureus*, *Bacillus subtilis*, *Escherichia coli*, *Corynebacterium*, *Pseudomonas aeruginosa*, etc. Taking into consideration the culture conditions and ethical factors, *S. aureus*, *B. subtilis*, and *E. coli* are selected for studying the antibacterial abilities of the nanocomposite. It is worth mentioning that to the best of our understanding, this study represents the first report on the versatile performances of the green-synthesized Fe_3O_4/CuO/CS nanocomposite in terms of its antibacterial efficacy against the mentioned microorganisms as well as its efficiency in selectively photodegrading MB dye.

2. MATERIALS AND METHODS

2.1. Chemicals. Iron(II) chloride tetrahydrate ($FeCl_2 \cdot 4H_2O$), iron(III) chloride hexahydrate ($FeCl_3 \cdot 6H_2O$), copper(II) nitrate trihydrate ($Cu(NO_3)_2 \cdot 3H_2O$), ammonia solution (NH_3), ethanol (C_2H_6O), chitosan (CS), dimethyl sulfoxide (DMSO), acetic acid (CH_3CO_2H), methylene blue ($C_{16}H_{18}ClN_3S \cdot xH_2O$), and nutrient agar were purchased from Merck KGaA (Darmstadt, Germany).

The following facilities are used in the process: Sonics & Materials VCX500 sonic bath (500 W, 20 kHz); heating mantle with magnetic stirring; pH meter; drying oven; glassware.

For the mangosteen extract preparation, dry mangosteen peels (*Garcinia mangostana* L.) were collected from the Southern region of Vietnam, washed with deionized water, and cold-dried. The cold, dry peels were chopped into small pieces. Approximately 30 g of them was placed in a Soxhlet extractor along with 300 mL of a mixture of ethanol and deionized water in a ratio of 1:1 (v/v) and left to work for 60 min. The extract was then cooled and filtered. The final solution was stored at a low temperature (8−10 °C) and used within 1 week.

The material properties were determined by scanning electron microscopy (SEM, Jeol-JMS), X-ray diffraction (XRD, PANalytical), vibrating sample magnetometry (VSM, Magnet B-10), and Fourier transform infrared (FTIR, Bruker) spectroscopy.

2.2. Synthesis of Fe_3O_4/CuO/CS Nanocomposites. The Fe_3O_4/CuO/CS nanocomposites were synthesized through a two-stage process.

Stage 1: Synthesis of Fe_3O_4 and CuO Nanoparticles. Fe_3O_4 NPs were formed by coprecipitation in an inert N_2 environment, according to our previously reported procedure.[23,24] CuO NPs were produced by the green synthesis method proposed by Adayabhanu.[25]

Fe_3O_4 NPs. A mixture of $FeCl_2 \cdot 4H_2O$ and $FeCl_3 \cdot 6H_2O$ with a Fe^{2+}/Fe^{3+} ratio of 1:2 was placed into a reaction flask and dissolved in 100 mL of deionized water. The reacting system was then heated and maintained at a temperature of 80 °C during the reaction. The mixture was stirred for 15 min and then sonicated with a probe intensity of 500 W and an amplitude of 40% at 5 s per pulse. At the same time, nitrogen gas was blown into the reaction flask and a 26−29% NH_3 solution was added dropwise to maintain the pH of the flask at 9−10. After the addition of the NH_3 solution, the mixture was continuously stirred for 15 min. The black precipitate product was collected by filtering in an external magnetic field (using a magnet). Afterward, the product was washed with deionized water until neutral pH and then rinsed two times using ethanol. Finally, the obtained material was left to dry overnight at a temperature of 60 °C.

CuO NPs. $Cu(NO_3)_2 \cdot 3H_2O$ was dissolved in 20 mL of mangosteen extract (see Section 2.1). The mixture was then kept at 400 ± 5 °C for 15 min. The obtained black precipitate was washed with distilled water, centrifuged, and dried at 100 °C for 3 h. Finally, the CuO NPs were stored in a dark container.

Stage 2: Ultrasound-Assisted Synthesis of Fe_3O_4/CuO/CS Nanocomposite. A 1% chitosan solution was prepared by adding 0.5 g of chitosan to 50 mL of 1 N acetic acid and sonicating for 15 min. Afterward, 2.5 g each of Fe_3O_4 and CuO were added to the solution. The mixture was then stirred for 0.5 h at a temperature of 60 °C. The resulting product was transferred to a Petri dish and left to dry for 24 h at a temperature of 60 °C.

2.3. Photocatalytic Degradation and Adsorption of MB. The MB adsorption and photocatalytic degradation ability of the composites were studied through experiments aimed at investigating the effects of the light conditions, pH, initial MB concentration, and Fe_3O_4/CuO/CS catalyst dose. In addition, we investigated the corresponding adsorption isotherm models. In all experiments, the removal efficiency was calculated as

$$H(\%) = \frac{C_o - C}{C_o} \times 100\% \quad (1)$$

where C_o and C are the concentrations of MB before and after irradiation in the photocatalytic reaction solution, respectively.[26]

2.4. Antibacterial Activity of Fe_3O_4/CuO/CS Nanocomposite. The preparation of nutrient agar plates involved the dissolution of 37.0 g of nutrient agar medium in 1000 mL of deionized water, followed by sterilization at 120 °C for 15 lbs/20 min. Then, the sterilized Petri dishes were filled with the nutrient agar medium and left to solidify. Subsequently, several pathogenic bacteria were cultured in the nutrient medium and distributed uniformly on the agar plate surface.

To evaluate the viability of the adhered microorganisms on the sample, the Fe_3O_4/CuO/chitosan sample and the CS reference material were sprinkled on Petri dishes containing the nutrient medium, followed by a viability test.

To determine the antibacterial ring diameter, the sample was dissolved in 1 mL of DMSO at a concentration of 200 μg/mL. Wells with a diameter of 5 ± 1 mm were then created in each sterile Petri dish. After that, 100 μL of CS or Fe_3O_4/CuO/CS dispersed in 10% DMSO solution, along with 100 μL of the standard antibiotic ampicillin (1 mg/mL), was added to the wells. The Petri dishes were then incubated at 37 °C for 24 h. After the specified incubation time, the diameters of the inhibition zones surrounding the wells were measured using a geometric Vernier caliper.

https://doi.org/10.1021/acsomega.3c04956
ACS Omega 2023, 8, 42429−42439

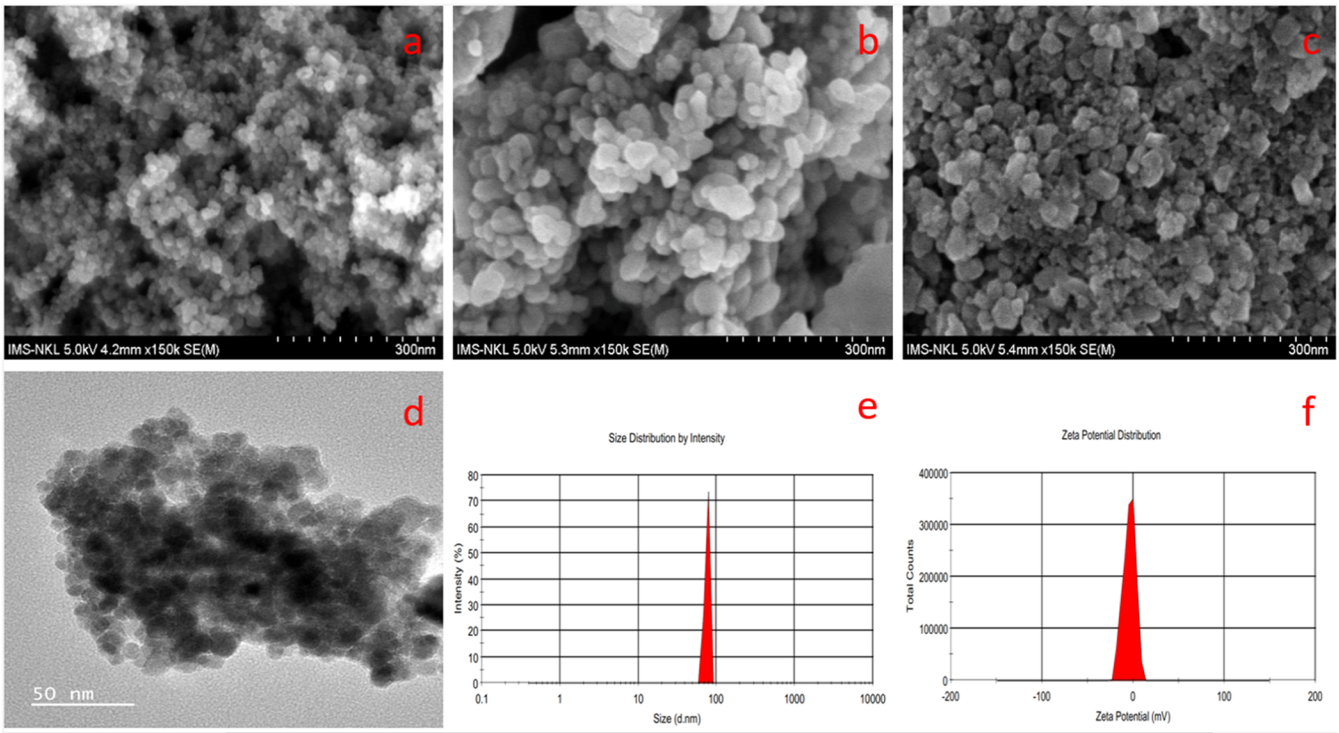

Figure 1. SEM images of Fe_3O_4 (a), CuO (b), and Fe_3O_4/CuO/CS (c). TEM image (d), size distribution (e), and ζ potential (f) of Fe_3O_4/CuO/CS.

Scheme 1. Schematic Illustration of Synthesis and Testing Procedures of Present Materials

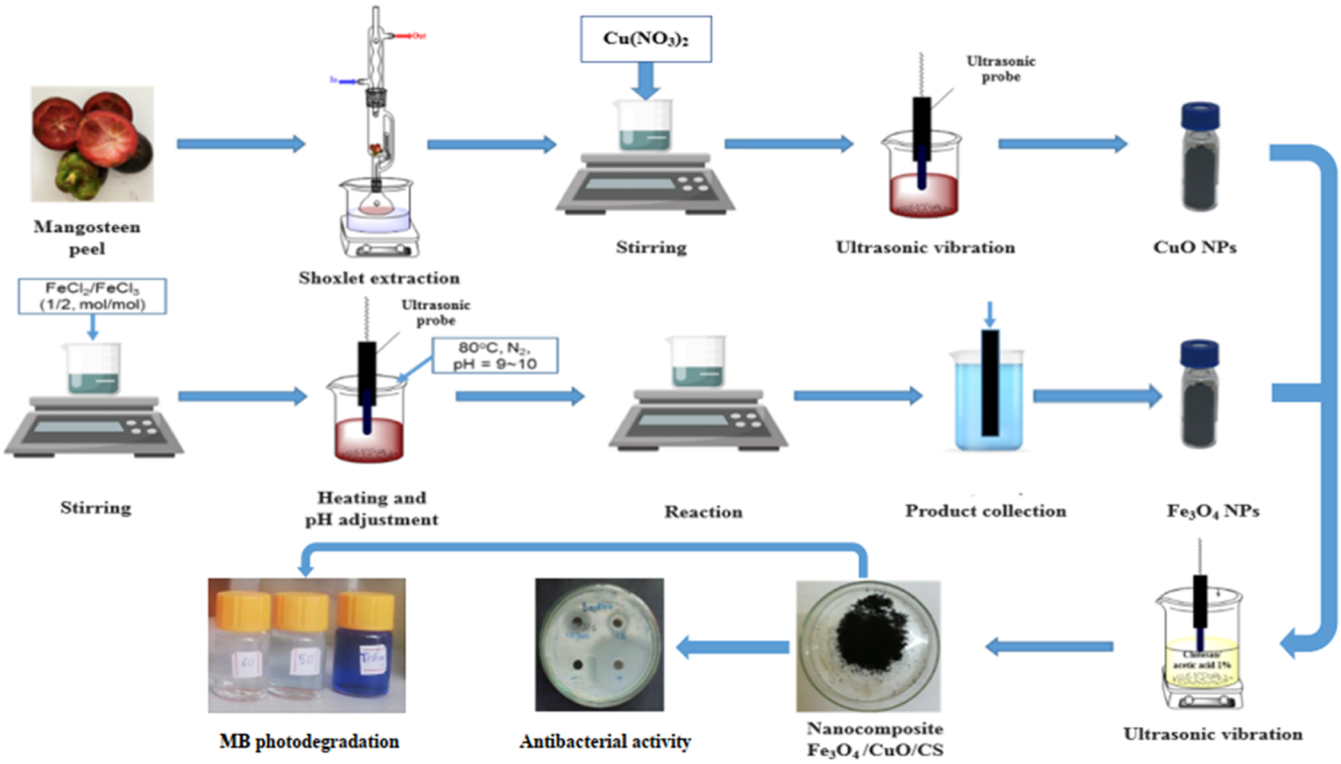

3. RESULTS AND DISCUSSION

3.1. Characterization of Fe_3O_4/CuO/CS Nanocomposite. The diameter and morphologies of Fe_3O_4, CuO, and Fe_3O_4/CuO/CS were investigated by using SEM. Figure 1a,b shows SEM images of Fe_3O_4 and CuO. The sizes of Fe_3O_4 and CuO NPs were 10−20 nm and 20−40 nm, respectively. Moreover, particle agglomeration was observed. This can be due to magnetic dipole−dipole interactions between the particles, the polarity of water during fabrication,[27] and the particular surface area of the NPs.[28] Moreover, Figure 1c shows that the nanocomposite materials exhibited fewer

https://doi.org/10.1021/acsomega.3c04956
ACS Omega 2023, 8, 42429−42439

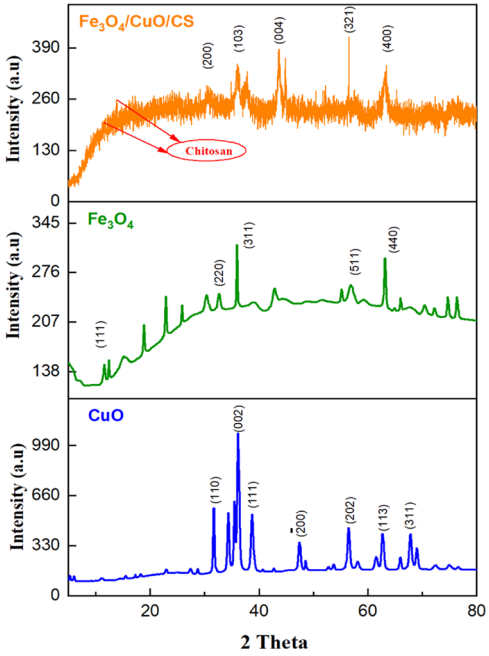

Figure 2. XRD patterns of Fe_3O_4/CuO/CS nanocomposite.

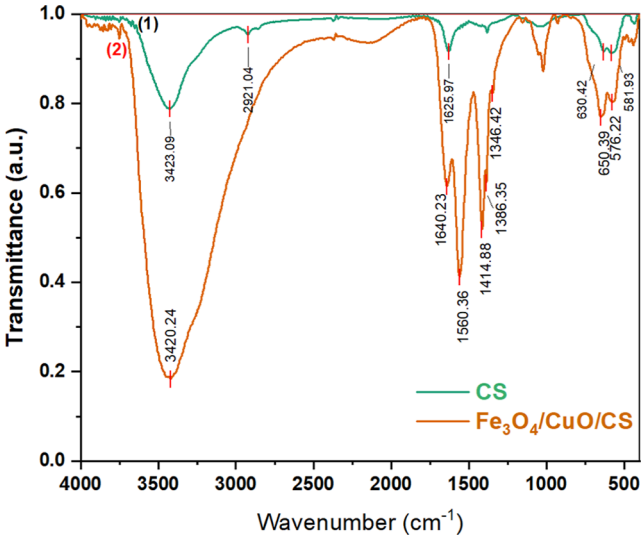

Figure 3. FT-IR spectra of the Fe_3O_4/CuO/CS nanocomposite and CS.

uniform sizes and a lower degree of agglomeration than Fe_3O_4 or CuO.

Some previous studies reported Fe_3O_4 and CuO coated with chitosan, which acted as a barrier layer, preventing the particles from moving toward each other (Scheme 1).[29,30]

In fact, the TEM image in Figure 1d shows that the Fe_3O_4/CuO nanoparticles had relatively uniform sizes and were surrounded by a chitosan layer. Additionally, the distribution of nano-oxides in the system directly affects the antibacterial ability, owing to the reactive oxygen species (ROS) reactions between the nanoparticles and the bacterial cell membrane.[31] Hence, we evaluated the size distribution of the nanocomposites shown in Figure 1e. The particles had an average size of 75.97 nm and a narrow size range, as confirmed by the SEM images discussed above. One way to assess the stability of a suspension is to analyze its ζ potential. This parameter

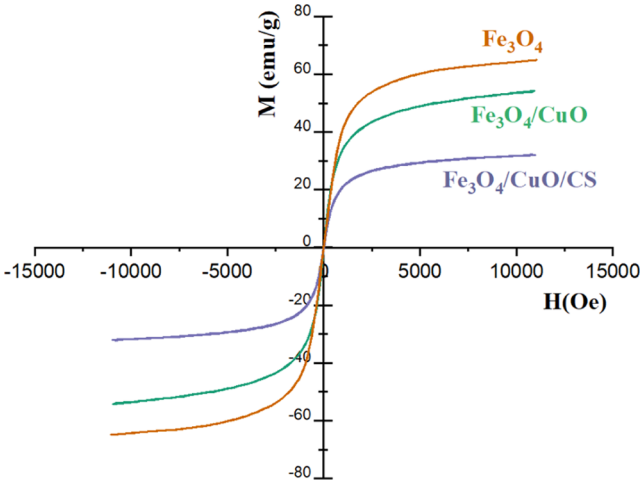

Figure 4. M−H curves of Fe_3O_4, Fe_3O_4/CuO, and Fe_3O_4/CuO/CS.

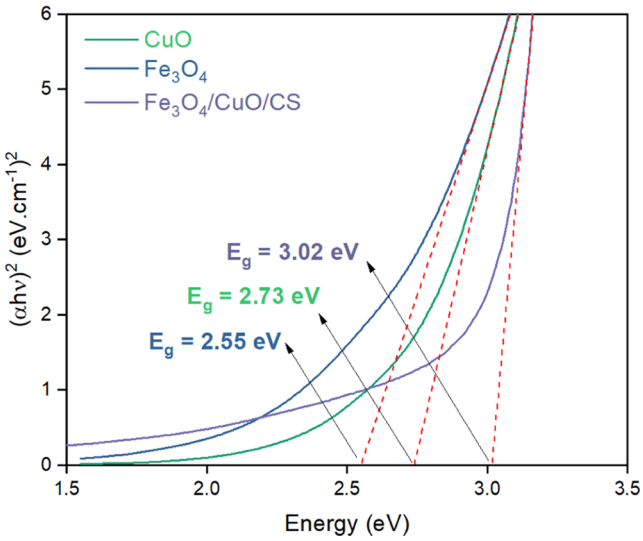

Figure 5. Bandgap energies of Fe_3O_4 NPs, CuO NPs, and the nanocomposite.

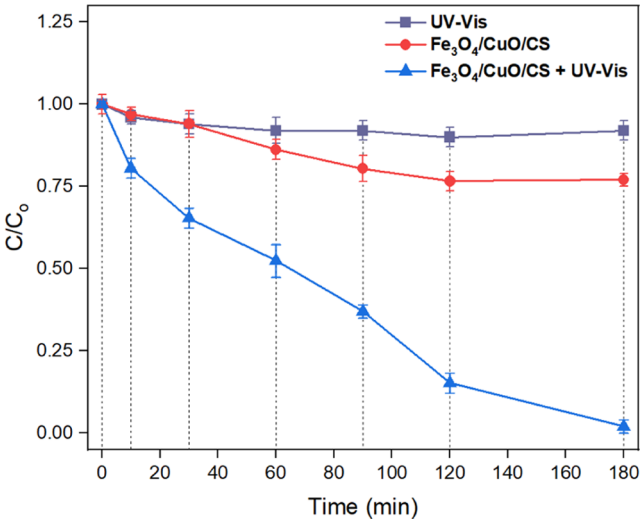

Figure 6. Effect of different light conditions on photocatalytic degradation.

https://doi.org/10.1021/acsomega.3c04956
ACS Omega 2023, 8, 42429−42439

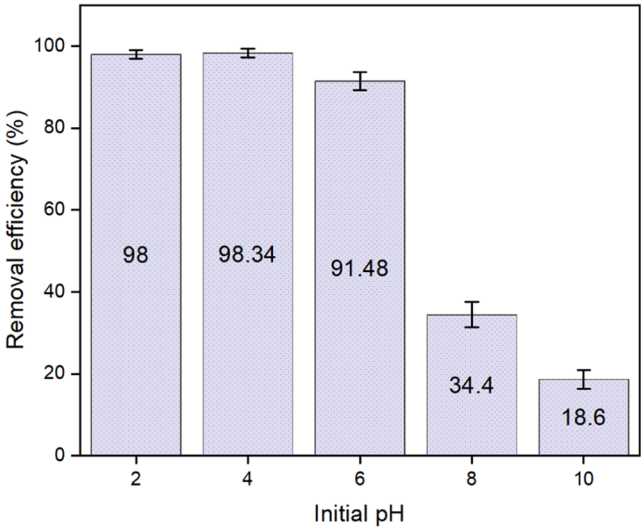

Figure 7. Effect of the Initial pH on photocatalytic degradation.

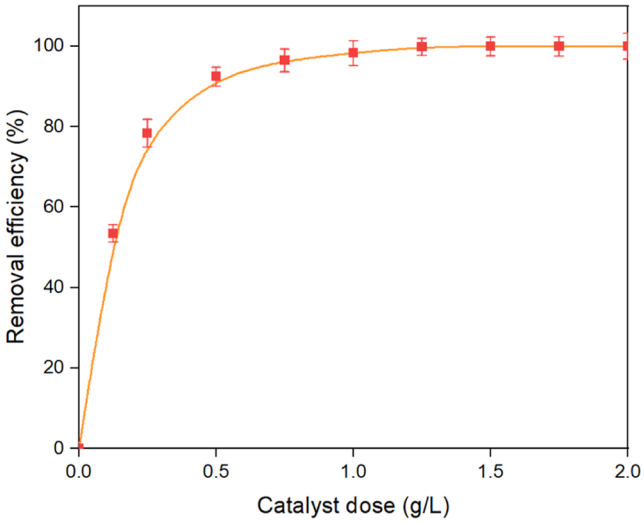

Figure 8. Effect of the Fe_3O_4/CuO/CS dose on the removal efficiency.

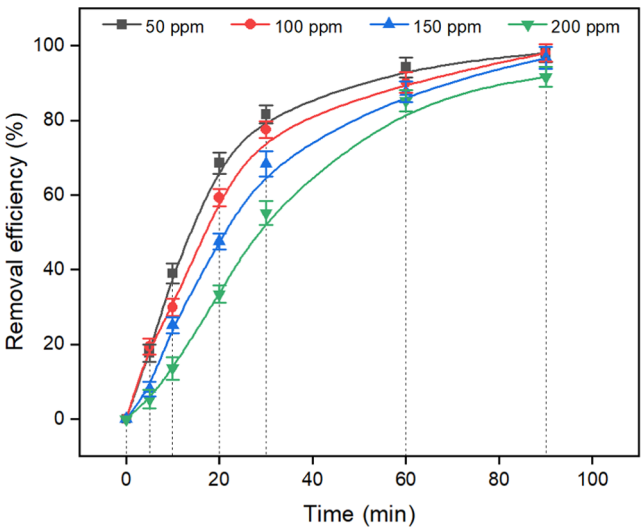

Figure 9. Effect of the initial MB concentration on removal efficiency.

depends on the surface charge of the particles in the suspension and the electrostatic forces between particles dispersed within it.[32] Figure 1f shows the measured ζ potential, with a negative surface charge of −4.36 mV; thus, a strong interaction would be present between the nanocomposite and Gram-positive bacteria.

The XRD pattern data (Figure 2) of the synthesized CuO (blue line) displayed several peaks related to the (110), (002), (111), (200), (202), (113), and (311) planes of the CuO monoclinic crystal structure (JCPDS 80-0076), with the strongest peak at 2θ = 36.14°, which corresponds to the (002) plane. The diffraction pattern of Fe_3O_4 in green coloration exhibited peak positions at 18.2, 35.4, 57.2, and 62.6°, which were identified as the (220), (511), and (440) planes, respectively.

Figure 3 shows the FT-IR spectrum of the Fe_3O_4/CuO/CS nanocomposite. The highest-intensity peak at 3243 cm^{-1} corresponded to a combination of symmetrical and asymmetrical modes of the stretching vibration of O−H bonds, as reported by Baghayeri.[33] The spectral peak observed at 1564 cm^{-1} can be attributed to the vibrational mode of the C═O functional group present in chitosan.[34] Notably, this peak exhibited the second highest intensity in the recorded spectrum. The spectral peaks observed at 653 and 579 cm^{-1} were attributed to the stretching vibrations of Cu−O and Fe−O groups, respectively.[35,36] The 1348 cm^{-1} peak was attributed to the deformation vibration of C−N groups,[37] whereas the peak of the primary alcohol groups (−C−O) of chitosan was found around 1418 cm^{-1}.[38] The peak observed at 1643 cm^{-1} could potentially correspond to the vibrational mode of C═O.[39]

Figure 4 shows the M−H curves of the nano-oxides and Fe_3O_4/CuO/CS nanocomposite samples at room temperature. It is well established that the magnetic properties have a great importance in biological applications.[40] The saturation magnetization (M_s) of the Fe_3O_4 NPs was 64.70 emu/g, which was two times higher than that of the nanocomposite (32.35 emu/g). The decrease may be due to the presence of the nonmagnetic CuO and chitosan materials. As CuO is an antiferromagnetic oxide at room temperature, it may reduce the magnetization and coercivity depending on its content.[41] Moreover, as discussed in the above morphological analysis, CS serves as a nonmagnetic coating layer on the exterior surface, which can impact consistency by suppressing the surface moments.[42]

The bandgap energies of the materials were calculated by utilizing the Tauc method based on UV−vis spectroscopy data. It can be seen from the data in Figure 5 that the bandgap energies of CuO NPs, Fe_3O_4 NPs, and Fe_3O_4/CuO/CS nanocomposite were 2.73, 2.55, and 3.02 eV, respectively. Therefore, further photocatalytic degradation experiments using the nanocomposite were conducted under sunlight and UV radiation.

3.2. Factors Affecting MB Dye Adsorption. *3.2.1. Effect of Light Conditions.* The effect of the light conditions was studied at a 50 mg·L^{-1} MB concentration and pH 4; three different conditions were explored. The first involved exposing the sample to UV light without any catalytic material, the second involved placing it in a dark chamber with a Fe_3O_4/CuO/CS dose of 1 g·L^{-1}, and the third involved exposing it to UV light with a dose of 1 g·L^{-1}. The data in Figure 6 show that UV light greatly enhanced the MB dye uptake of Fe_3O_4/CuO/CS. Moreover, the MB degradation rate was relatively low

https://doi.org/10.1021/acsomega.3c04956
ACS Omega 2023, 8, 42429−42439

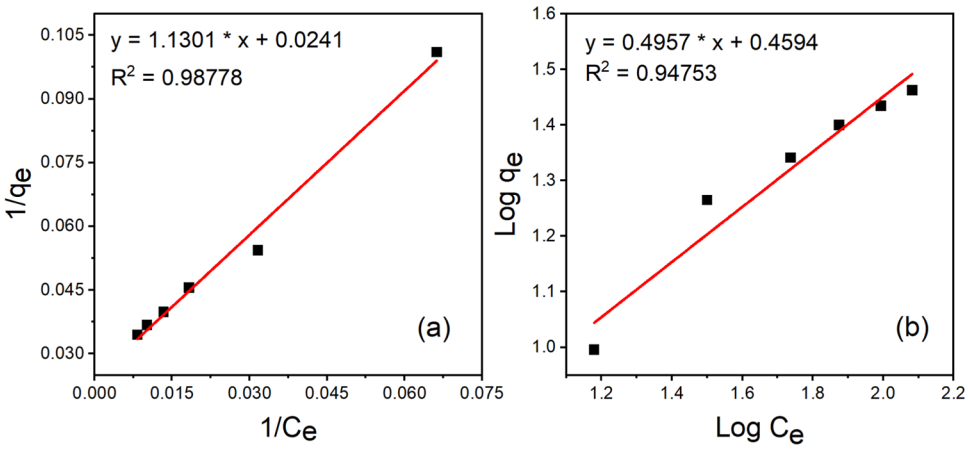

Figure 10. Langmuir (a) and Freundlich (b) isotherm analysis.

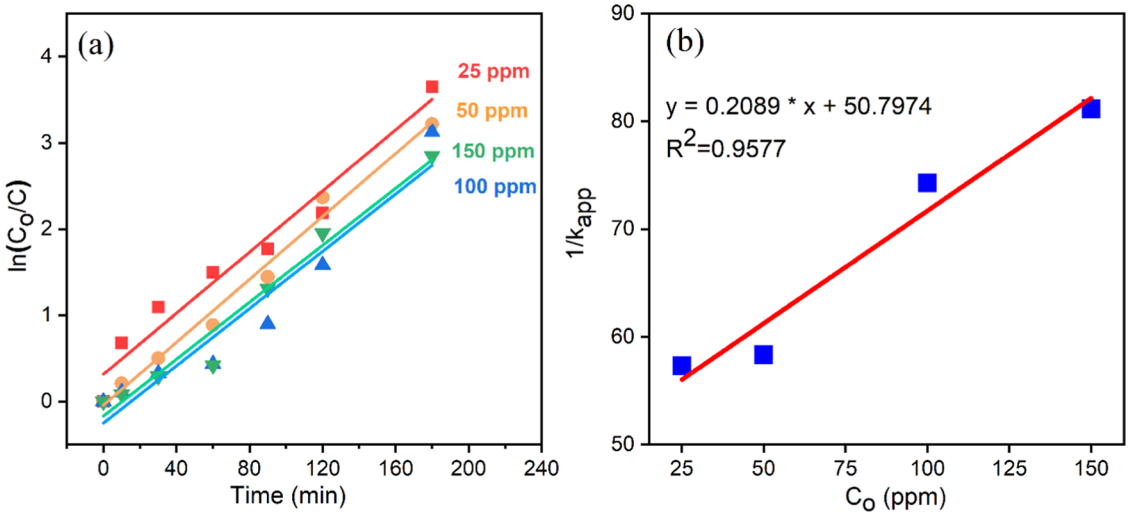

Figure 11. Pseudo-first-order model for MB adsorption and the relationship between initial MB concentration and reciprocal of the rate constant.

Table 1. Kinetic Parameters for the Adsorption Process

C_o (ppm)	R^2	kinetic equation	k_{app} (min^{-1})	k_f (mg $L^{-1}min^{-1}$)	K_{LH} (L mg^{-1})
25	0.91524	$y = 0.01772x + 0.31424$	0.01772	23.58490	0.00078
50	0.98732	$y = 0.01825x - 0.04444$	0.01825		
100	0.92343	$y = 0.01661x - 0.25232$	0.01661		
150	0.96876	$y = 0.01652x - 0.1709$	0.01652		

(23%) when only the adsorbent material was present (in dark conditions) or under normal UV irradiation (8%). For this reason, UV light was selected for the subsequent analyses.

3.2.2. Effect of Initial pH. Another significant factor influencing the photocatalytic activity is the initial pH. The relationship between the MB removal efficiency of the nanocomposite and the pH value (in the 2−10 range) was investigated with an initial MB concentration of 50 mg·L^{-1} (1 g·L^{-1} Fe_3O_4/CuO/CS) under UV light irradiation for 180 min. Surprisingly, the removal efficiency reached its highest value of 98.34% at pH 4 and fell sharply at basic pH (8−10), as shown in Figure 7. This result is in contrast to some previous studies, in which a low MB degradation percentage was often observed under acidic conditions. It has been reported that, in a basic medium, the prevalence of negative charges on the surface of the adsorbent enhances the electrostatic attraction for the cationic MB dye, facilitating its adsorption.[43] On the

Figure 12. Colors of dyes before photodegradation, after one cycle, and after five cycles.

https://doi.org/10.1021/acsomega.3c04956
ACS Omega 2023, 8, 42429−42439

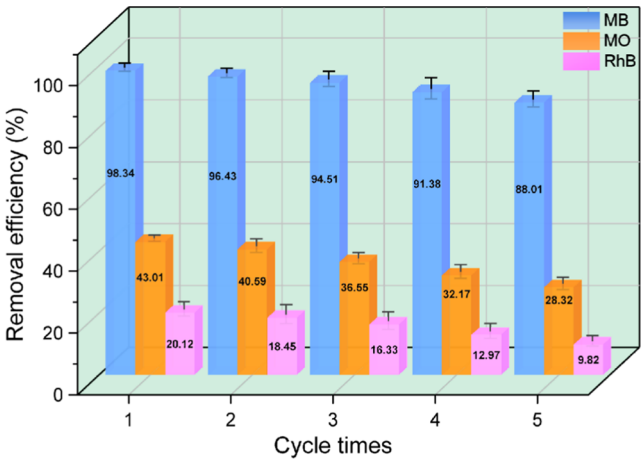

Figure 13. Photodegradation efficiency of the catalyst for dyes after five cycles.

Table 2. Comparison of the Photodegradation Efficiency with the Literature Reports

materials	*H*% (dose)	dyes (conc.)	year[ref]
CS/PANI/Fe_3O_4	96.16% (3 g/L)	reactive red 198 (50 ppm)	2020[49]
Gr/CS/Fe_3O_4	100% (5 g/L)	RhB (10^{-5} M)	2020[50]
PANI@CS-GO-OXS/CuO	94% (1 g/L)	RhB (2×10^{-5} M)	2021[51]
$WO_{2.72}/Fe_3O_4$	96.55% (0.3 g/L)	RhB (20 ppm)	2020[52]
	95% (0.3 g/L)	MB (20 ppm)	
Fe_3O_4/CuO/CS	98.34% (1 g/L)	MB (50 ppm)	this work
	43.01% (1 g/L)	MO (50 ppm)	
	20.12% (1 g/L)	RhB (50 ppm)	

Table 3. Bandgap Energy, Electronegativity, CB, and VB Potentials of Prepared Samples

	E_g (eV)	χ (eV)	E_{CB} (eV)	E_{VB} (eV)
Fe_3O_4	2.55	5.76	−0.015	2.535
CuO	2.73	5.81	−0.055	2.675
Fe_3O_4/CuO/CS	3.02	5.77	−0.240	2.780

other hand, under acidic conditions, the adsorbent surface exhibits a positive charge, resulting in electrostatic repulsion of the cationic adsorbate and hindering its adsorption.[44] This difference might be due to the presence of other important interactions comparable to electrostatic interactions, such as H-bonding, hydrophobic and hydrophilic interactions, and van der Waals forces.[45] On the other hand, the MB uptake percentage at pH 4 was higher than that at pH 2, possibly due to the dissolution of Fe_3O_4 nanoparticles.[46] Hence, pH 4 was chosen for further investigation.

3.2.3. Effect of Fe_3O_4/CuO/CS Nanocomposites Dose. We then assessed the impact of the catalyst dose on the removal efficiency under the following conditions: UV light exposure, an initial MB concentration of 50 mg·L^{-1}, pH 4, and a contact time of 180 min. As illustrated in Figure 8, the degradation rate increased with an increasing catalyst dose. When the concentration of the catalyst exceeded 1.0 g·L^{-1}, the degradation rate increased to around 98%. Therefore, an ideal catalyst dose of 1.0 g·L^{-1} was chosen for the subsequent experiments.

3.2.4. Effect of Initial MB Concentration. Next, we evaluated the effect of the initial MB concentration. According to recent research, the initial dye concentration can affect the availability of binding sites on the adsorbent, which influences the efficiency of dye removal.[45] The effect was studied after 90 min under the following conditions: pH of 4.0, a Fe_3O_4/CuO/CS dose of 1.0 g·L^{-1}, and different MB concentrations (50, 100, 150, and 200 ppm). The data in Figure 9 show that, for all initial concentrations, the MB removal rate reached 91% or more after 90 min. Typically, as the initial dye concentration increases, the adsorption sites on the surface of the adsorbent will become occupied, leading to saturation and ultimately resulting in a decline in the efficiency of the removal process.[43] However, the difference in MB removal efficiency among the three concentrations was not significant. Additional investigations were conducted on the isotherm model and adsorption kinetics of the MB dye, specifically at an initial concentration of 50 ppm.

3.3. Adsorption Isotherm Analysis. The linear fits of the isotherm equations in Figure 10 show that the Langmuir model, with a correlation coefficient (R^2) of 0.98778, provided a more accurate description of the phenomenon compared to that of the Freundlich model (R^2 = 0.94753). This result suggests that monolayer adsorption of MB occurred on the surface of the nanocomposites.

The maximum adsorption capacity q_{max} (mg·g^{-1}) and the Langmuir constant K_L (L·mg^{-1}) were thus calculated from the Langmuir isotherm model equation:

$$C_e/q_e = (1/q_{max})C_e + [1/(q_{max} \times K_L) \quad (2)$$

where C_e and q_e are the equilibrium concentration (mg/L) and adsorbed quantity (mg/g) of MB per unit mass of adsorbent, respectively.[47] The obtained q_{max} and K_L values were 41.49 mg·g^{-1} and 2.1×10^{-2} L·mg^{-1}, respectively.

3.4. Kinetic Analysis. As illustrated in Figure 11a, the degradation process followed a pseudo-first-order kinetic model, as evidenced by the direct correlation between $\ln(C_0/C)$ and adsorption time. The corresponding k values were calculated by linear regression. The values of k and the linear regression coefficients R^2 obtained for different initial MB concentrations are summarized in Table 1. Furthermore, Figure 11b shows the relationship between the initial MB concentration and the reciprocal of the rate constant ($1/k_{app}$), which exhibited the expected linear relationship. The obtained data confirmed the pseudo-first-order mechanism of the reaction, with R^2 values ranging from 0.91524 to 0.98732. The adsorption constant (K_L) of the kinetic model was found to be similar to the value obtained in the absence of light, with $K_L = 32.051 \times K_{LH}$. Additionally, the photocatalyzed decomposition of MB at the initial dose of 150 mg·L^{-1}, pH 4.0, and 1 g·L^{-1} catalyst dose followed the Langmuir–Hinshelwood model. Other studies reported similar results, with the K_{LH} constant measured during irradiation being significantly different from the K_L value measured in the absence of light.[48]

3.5. Reusability and Selectivity. Selectivity experiments were performed using Methyl Orange (MO = anionic) and Rhodamine B (RhB = cationic) dyes under the same conditions as those applied for MB. Additionally, assessments were made regarding the nanocomposite's reusability with the use of these dyes. After each experiment, the nanocatalysts

https://doi.org/10.1021/acsomega.3c04956
ACS Omega 2023, 8, 42429−42439

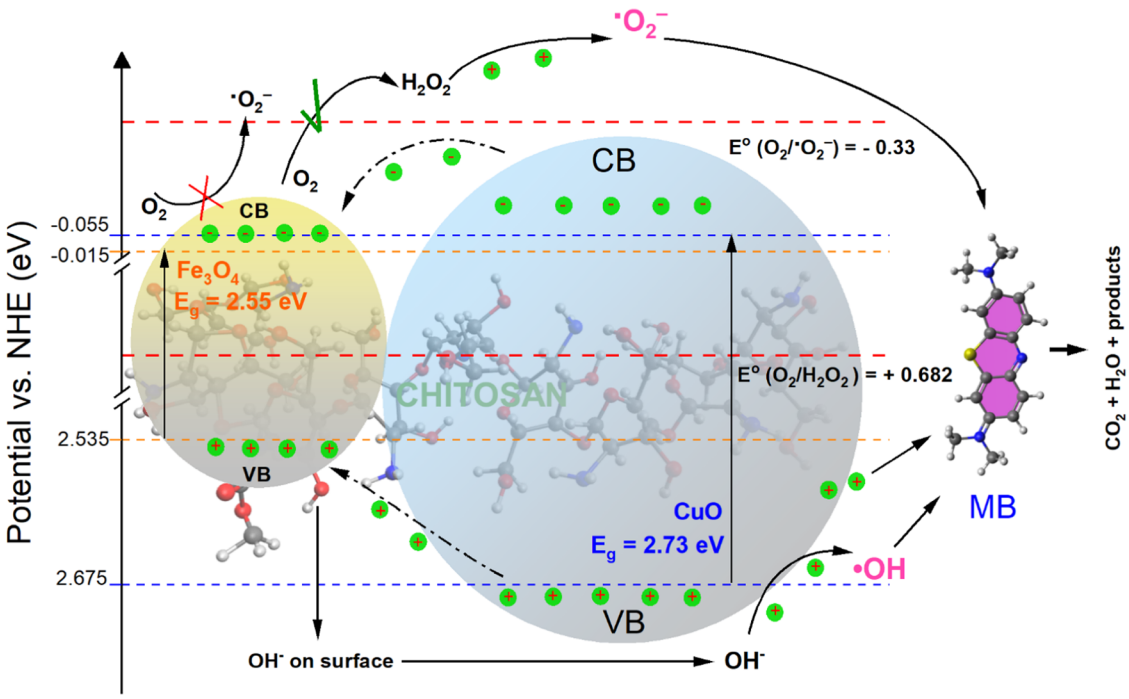

Figure 14. Photodegradation efficiency of the catalyst for dyes after five cycles.

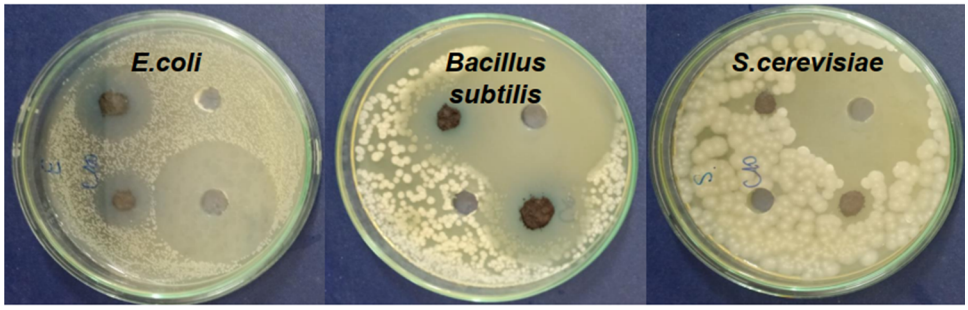

Figure 15. Investigation of antibacterial activity against *E. coli*, *B. subtilis*, and *S. cerevisiae*.

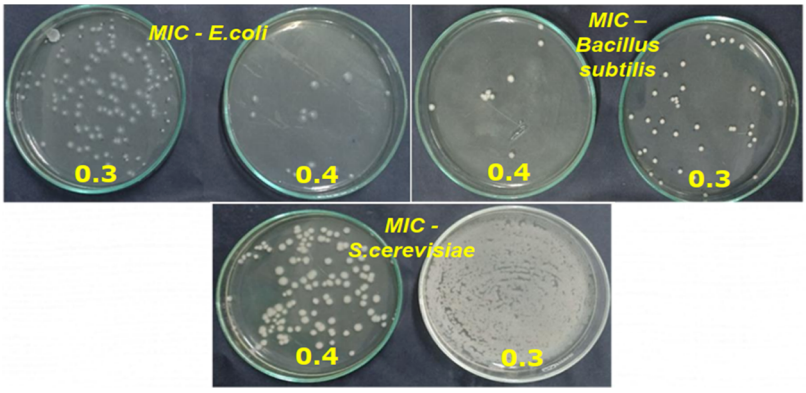

Figure 16. Antibacterial activity of Fe_3O_4/CuO/CS at different concentrations.

were isolated using a magnetic field, rinsed with absolute alcohol, dried, and subsequently employed for further testing. The outcomes of these experiments are illustrated in Figures 12 and 13.

In general, the nanocomposites exhibit an acceptable reusability. Figure 13 illustrates that after five cycles, the adsorption efficiency for MB remains at 88.01%, representing a decrease of roughly 10% compared to the performance in the initial cycle. Similarly, the efficiency for MO and RhB decreases by approximately 15 and 10%, respectively, reaching 28.32 and 9.82%. Furthermore, Figure 12 presents evidence that the fading of RhBis is less pronounced, despite sharing the same cationic dye classification as MB. This result indicates the novel material's high selectivity for MB dye in the photodegradation process. The comparison of the photodegradation

https://doi.org/10.1021/acsomega.3c04956
ACS Omega 2023, 8, 42429−42439

Table 4. Diameters of Antibacterial Ring of Fe_3O_4/CuO/CS Material

microorganism	diameter (mm ±0.1)	
	30 mg	60 mg
E. coli	12	18
B. subtilis	10	16
S. cerevisiae	12	16

efficiency of the nanocomposite with various materials based on Fe_3O_4, CuO, and CS is presented in Table 2.

3.6. Possible Photocatalytic Mechanism. To elucidate the segregation of photogenerated electron−hole pairs within the ternary nanocomposites, it becomes absolutely necessary to determine the conduction band (CB) and valence band (VB) potentials of the constituent elements. The following equations were utilized to compute these energy levels:[53]

$$\chi_{A_aB_b} = [\chi_A{}^a \chi_B{}^b]^{1/a+b} \quad (3)$$

$$E_{CB} = \chi - E^e - 0.5E_g \quad (4)$$

$$E_{VB} = E_{CB} + E_g \quad (5)$$

where χ (eV), E_{CB} (eV), E_{VB} (eV), and E_g (eV) are the Mulliken's absolute electronegativity, the CB edge potential, the VB edge potential, and the bandgap energy of the semiconductors, respectively. Additionally, parts a and b correspond to the numbers of atoms in the chemical formula A_aB_b. E^e is the energy of free electrons on the hydrogen scale (4.5 eV). The values of χ and E_g for Fe_3O_4 are 5.76 and 2.55 eV, respectively. Hence, its E_{CB} and E_{VB} are calculated to be −0.015 and 2.535 eV, respectively, relative to those of the normal hydrogen electrode (NHE). The parameters for CuO and Fe_3O_4/CuO/CS are also measured and are shown in Table 3.

Figure 14 depicts the possible mechanism for photodegradation. It is widely acknowledged that both Fe_3O_4 and CuO have the capability to absorb photons and generate electron−hole pairs upon light exposure. The CB potentials for Fe_3O_4 and CuO, which are −0.015 and −0.055 eV vs NHE, respectively, are higher than the standard redox potential (E^o) of $O_2/{}^\bullet O_2^-$ (−0.33 eV vs NHE). This suggests that the electrons (e^-) can transition from the CB of CuO to the CB of Fe_3O_4 but are incapable of reducing O_2 to ${}^\bullet O_2^-$ radicals.[54] However, these electrons can be transferred to adsorbed oxygen molecules, resulting in the formation of H_2O_2, since the CB levels of Fe_3O_4 and CuO have a more negative potential than E^0 of O_2/H_2O_2 (+0.682 eV vs NHE).[53] The H_2O_2 molecules are then prompted to generate the ${}^\bullet O_2^-$ radicals by the presence of holes.[55]

Furthermore, the VB potential of Fe_3O_4 (2.535 eV vs NHE) is lower than that of CuO (2.675 eV vs NHE) but surpasses the E^o of ${}^\bullet OH/OH^-$ (2.38 eV vs NHE). Consequently, the photoexcited holes (h^+) within the VB of Fe_3O_4 can oxidize OH^- on the surface of the nanocomposites, leading to the production of ${}^\bullet OH$ radicals.[56] Finally, the ${}^\bullet O_2^-$, ${}^\bullet OH$, and h^+ species will directly react with MB molecules and degrade them into CO_2, H_2O, and other products.[57]

3.7. Antibacterial Activity. Figure 15 shows that the Fe_3O_4/CuO/CS samples had better inhibitory activity against *B. subtilis* and *E. coli* than against *Saccharomyces cerevisiae*; *E. coli* , *B. subtilis*, and *S. cerevisiae* each had MIC values of 0.3, 0.3, and 0.4 mg/mL, respectively (Figure 16). Moreover, we tested a sample in contact with the control microorganism suspension (with a large number of microorganisms) on the control plates (the nutrient medium plates were evenly filled with the microorganism suspension and not treated with the test material sample), and the microorganisms were observed to grow in a thick, smooth layer.

The measured antibacterial diameters of the Fe_3O_4/CuO/CS samples at two different concentrations of the tested microorganisms are presented in Table 4. The antibacterial ability of the Fe_3O_4/CuO/CS system is the combined effect of each component present in the nanocomposite including metal oxide and chitosan. Fe_3O_4 and CuO nanoparticles are known to interact with microbial cell membranes, causing disruption to DNA replication, cell division, and cellular respiration. This leads to an expansion of the surface area of the cell, ultimately causing its destruction.[44] Chitosan has strong antibacterial properties against both Gram bacteria in acidic media, according to a few earlier papers.[37,38] The Fe_3O_4/CuO/CS nanocomposites showed higher antibacterial activity against *B. subtilis* than against *E. coli* and inhibited the growth of *S. cerevisiae* yeast cells.

4. CONCLUSIONS

Fe_3O_4/CuO/CS materials were successfully synthesized by an ultrasound-assisted green method. The experiments assessing the adsorption efficiency of the catalysts with MB, MO, and RhB revealed a high degree of selective photodegradation with MB (reaching approximately 98% after 180 min). The adsorption isotherm with MB dye was consistent with the Langmuir model (R^2 = 0.987), and the adsorption constant (K_{LH}) was significantly different from the Langmuir constant (K_L). The potential photodegradation mechanism of Fe_3O_4/CuO/CS was investigated, with ${}^\bullet O_2^-$, ${}^\bullet OH$, and h^+ playing crucial roles in the photoreaction. Furthermore, the remarkable reusability of the novel material further justified its suitability for environmental applications. The strong antibacterial activities of the nanocomposite have also been confirmed through the discovery of their minimal inhibitory concentrations for *S. cerevisiae*, *B. subtilis*, and *E. coli*, which were measured at 0.4, 0.3, and 0.4 mg/mL, respectively. This study has presented promising results regarding the multiapplication potential of the synthesized material; however, the selective photodegradation mechanism between cationic dyes such as MB and RhB needs further elucidation in subsequent studies.

■ AUTHOR INFORMATION

Corresponding Author

Nguyen Thi Huong − *Institute of Chemistry and Materials, Ha Noi 100000, Vietnam*; orcid.org/0000-0003-2716-936X; Email: nguyenhuong0916@gmail.com

Authors

Pham Thi Mai Huong − *Hanoi University of Industry, Ha Noi 100000, Vietnam*

Nguyen Thi Kim Giang − *Faculty of Chemistry, Hanoi National University of Education, Hanoi 100000, Vietnam*

Phung Thi Lan − *Faculty of Chemistry, Hanoi National University of Education, Hanoi 100000, Vietnam*

Vu Thanh Dong − *Institute of Chemistry and Materials, Ha Noi 100000, Vietnam*

Cong Tien Dung − *Hanoi University of Mining and Geology, Hanoi 100000, Vietnam*

Complete contact information is available at:

https://doi.org/10.1021/acsomega.3c04956
ACS Omega 2023, 8, 42429−42439

https://pubs.acs.org/10.1021/acsomega.3c04956

Notes

The authors declare no competing financial interest.

■ ACKNOWLEDGMENTS

The authors thank the Institute of Chemistry and Materials for the support of this work.

■ REFERENCES

(1) Sin, J.-C.; Lam, S.-M.; Zeng, H.; Lin, H.; Li, H.; Huang, L.; Tham, K.-O.; Mohamed, A. R.; Lim, J.-W. Enhanced synchronous photocatalytic 4-chlorophenol degradation and Cr(VI) reduction by novel magnetic separable visible-light-driven Z-scheme CoFe2O4/P-doped BiOBr heterojunction nanocomposites. *Environ. Res.* **2022**, *212*, No. 113394.

(2) Zhao, L.; Lam, S.-M.; Ong, Y. T.; Sin, J.-C.; Zeng, H.; Xie, Q.; Lim, J. W. Fe2WO6 coupling on cube-like SrTiO3 as a highly active S-scheme heterojunction composite for visible light photocatalysis and antibacterial applications. *Environ. Technol. Innovation* **2022**, *28*, No. 102941.

(3) Sin, J. C.; Lam, S. M.; Zeng, H.; Lin, H.; Li, H.; Huang, L.; Liaw, S. J.; Mohamed, A. R.; Lim, J. W. Construction of visible light-driven Eu-doped BiOBr hierarchical microflowers for ameliorated photocatalytic 2,4-dichlorophenol and pathogens decomposition with synchronized hexavalent chromium reduction. *Mater. Today Sustainability* **2023**, *22*, No. 100340.

(4) Das, D.; Nath, B. C.; Phukon, P.; Dolui, S. K. J. C.; Biointerfaces, S. B. Synthesis and evaluation of antioxidant and antibacterial behavior of CuO nanoparticles. *Colloids Surf., B* **2013**, *101*, 430−433.

(5) Prabhu, Y.; Rao, K. V.; Kumari, B. S.; Kumar, V. S. S.; Pavani, T. Synthesis of Fe3O4 nanoparticles and its antibacterial application. *Int. Nano Lett.* **2015**, *5* (2), 85−92.

(6) Lam, S.-M.; Choong, M.-K.; Sin, J.-C.; Zeng, H.; Huang, L.; Hua, L.; Li, H.; Jaffari, Z. H.; Cho, K. H. Construction of delaminated Ti3C2MXene/NiFe2O4/V2O5 ternary composites for expeditious pollutant degradation and bactericidal property. *J. Environ. Chem. Eng.* **2022**, *10* (5), No. 108284.

(7) Dehdashtian, S.; Gholivand, M. B.; Shamsipur, M. Construction of a sensitive and selective sensor for morphine using chitosan coated Fe3O4 magnetic nanoparticle as a modifier. *Mater. Sci. Eng., C* **2016**, *58*, 53−59, DOI: 10.1016/j.msec.2015.07.049.

(8) Ou, G.; Fan, P.; Ke, X.; Xu, Y.; Huang, K.; Wei, H.; Yu, W.; Zhang, H.; Zhong, M.; Wu, H. Defective molybdenum sulfide quantum dots as highly active hydrogen evolution electrocatalysts. *Nano Res.* **2018**, *11* (2), 751−761.

(9) Yong, Z.-J.; Lam, S.-M.; Sin, J.-C.; Zeng, H.; Mohamed, A. R.; Jaffari, Z. H. Boosting sunlight-powered photocatalytic fuel cell with S-scheme Bi2WO6/ZnO nanorod array composite photoanode. *Inorg. Chem. Commun.* **2022**, *143*, No. 109826.

(10) Thanh, V. M.; Huong, N. T.; Dung, N. D. T.; Nguyen-Le, M.-T. Synthesis of Ternary Fe3O4/ZnO/Chitosan Magnetic Nanoparticles via an Ultrasound-Assisted Coprecipitation Process for Antibacterial Applications. *J. Nanomater.* **2020**, *2020*, No. 8875471, DOI: 10.1155/2020/8875471.

(11) Lemine, O.; Omri, K.; Zhang, B.; El Mir, L.; Sajieddine, M.; Alyamani, A.; Bououdina, M. Sol−gel synthesis of 8 nm magnetite (Fe3O4) nanoparticles and their magnetic properties. *Superlattices Microstruct.* **2012**, *52* (4), 793−799.

(12) Saito, G.; Hosokai, S.; Tsubota, M.; Akiyama, T. Synthesis of copper/copper oxide nanoparticles by solution plasma. *J. Appl. Phys.* **2011**, *110* (2), No. 023302.

(13) Pham, T. M. H.; Vu, M. T.; Cong, T. D.; Nguyen, N. S.; Doan, T. A.; Truong, T. T.; Nguyen, T. H. Green sonochemical process for preparation of polyethylene glycol−Fe 3 O 4/ZnO magnetic nanocomposite using rambutan peel extract as photocatalyst, for removal of methylene blue in solution. *Bull. Mater. Sci.* **2022**, *45* (1), No. 13.

(14) John, M. S.; Nagoth, J. A.; Zannotti, M.; Giovannetti, R.; Mancini, A.; Ramasamy, K. P.; Miceli, C.; Pucciarelli, S. Biogenic synthesis of copper nanoparticles using bacterial strains isolated from an antarctic consortium associated to a psychrophilic marine ciliate: Characterization and potential application as antimicrobial agents. *Mar. Drugs* **2021**, *19* (5), No. 263.

(15) Mallakpour, S.; Mansourzadeh, S. Sonochemical synthesis of PVA/PVP blend nanocomposite containing modified CuO nanoparticles with vitamin B1 and their antibacterial activity against *Staphylococcus aureus* and *Escherichia coli*. *Ultrason. Sonochem.* **2018**, *43*, 91−100.

(16) No, H. K.; Park, N. Y.; Lee, S. H.; Meyers, S. P. Antibacterial activity of chitosans and chitosan oligomers with different molecular weights. *Int. J. Food Microbiol.* **2002**, *74* (1−2), 65−72.

(17) Wu, Y.; Wang, Y.; Luo, G.; Dai, Y. In situ preparation of magnetic Fe3O4-chitosan nanoparticles for lipase immobilization by cross-linking and oxidation in aqueous solution. *Bioresour. Technol.* **2009**, *100* (14), 3459−3464.

(18) Chang, Y.-C.; Chen, D.-H. Preparation and adsorption properties of monodisperse chitosan-bound Fe3O4 magnetic nanoparticles for removal of Cu (II) ions. *J. Colloid Interface Sci.* **2005**, *283* (2), 446−451.

(19) Thi Huong, N.; Son, N. N.; Phuong, V. H.; Dung, C. T.; Huong, P. T. M.; Son, L. T. Technology, Synthesis Fe3O4/Talc nanocomposite by coprecipition-ultrasonication method and advances in hexavalent chromium removal from aqueous solution. *Adsorpt. Sci. Technol.* **2020**, *38* (9−10), 483−501.

(20) Taufiq, A.; Saputro, R. E.; Susanto, H.; Hidayat, N.; Sunaryono, S.; Amrillah, T.; Wijaya, H. W.; Mufti, N.; Simanjuntak, F. M. Synthesis of Fe_{3O4}/Ag nanohybrid ferrofluids and their applications as antimicrobial and antifibrotic agents. *Heliyon* **2020**, *6* (12), No. e05813, DOI: 10.1016/j.heliyon.2020.e05813.

(21) Guan, G.; Zhang, L.; Zhu, J.; Wu, H.; Li, W.; Sun, Q. Antibacterial properties and mechanism of biopolymer-based films functionalized by CuO/ZnO nanoparticles against *Escherichia coli* and *Staphylococcus aureus*. *J. Hazard. Mater.* **2021**, *402*, No. 123542.

(22) El-Gharably, A. A.; Kenawy, E.-R. S.; Safaan, A. A.; Aboamna, S. A.; Mahmoud, Y. A. G.; Mandour, H. S. A. Synthesis, characterization and application of chitosan conjugated heterocyclic compounds. *J. Polym. Res.* **2022**, *29* (4), No. 141.

(23) Nguyen, T.; Le, N.; Cong, T.; Nguyen, N.; Nguyen, D.; Dao, T.; Vu, M. Effect of ultrasonication time and peg content on the crystallite size and lattice parameter of polyethylene glycol (peg)-coated Fe3O4 nanoparticles synthesized by a ultrasound assiste co-precipitation process. *Vietnam J. Chem.* **2019**, *57*, 340−346.

(24) Vu, M.; Dao, T.; Pham, T.; Pham, T.; Cong, T.; Nguyen, N.; Nguyen, T. Modified iron oxide nanoparticles with polyethylene glycol and citric acid for biomedical applications. *Vietnam J. Chem.* **2019**, *57*, 365−371.

(25) Udayabhanu; Nethravathi, P. C.; Pavan Kumar, M. A.; Lingaraju, K.; Rajanaika, H.; Nagabhushana, H.; Sharma, S. C. Tinospora cordifolia mediated facile green synthesis of cupric oxide nanoparticles and their photocatalytic, antioxidant and antibacterial properties. *Mater. Sci. Semicond. Process.* **2015**, *33*, 81−88, DOI: 10.1016/j.mssp.2015.01.034.

(26) Atla, S. B.; Lin, W.-R.; Chien, T.-C.; Tseng, M.-J.; Shu, J.-C.; Chen, C.-C.; Chen, C.-Y. Fabrication of Fe3O4/ZnO magnetite core shell and its application in photocatalysis using sunlight. *Mater. Chem. Phys.* **2018**, *216*, 380−386.

(27) Tran, T. H.; Nguyen, V. T. Copper Oxide Nanomaterials Prepared by Solution Methods, Some Properties, and Potential Applications: A Brief Review. *Int. Scholarly Res. Not.* **2014**, *2014*, No. 856592.

(28) Yu, C.; Gou, L.; Zhou, X.; Bao, N.; Gu, H. Chitosan−Fe3O4 nanocomposite based electrochemical sensors for the determination of bisphenol A. *Electrochim. Acta* **2011**, *56* (25), 9056−9063.

(29) Zayed, M. F.; Eisa, W. H.; Hosam, A. E. M.; Abou Zeid, A. M. Spectroscopic investigation of chitosan-supported Cu2O/CuO nano-

composite; a separable catalyst for water-pollutants degradation. *J. Alloys Compd.* **2020**, *835*, No. 155306.
(30) Zhao, D.-L.; Wang, X.-X.; Zeng, X.-W.; Xia, Q.-S.; Tang, J.-T. Preparation and inductive heating property of Fe3O4−chitosan composite nanoparticles in an AC magnetic field for localized hyperthermia. *J. Alloys Compd.* **2009**, *477* (1), 739−743.
(31) Yamamoto, O. Influence of particle size on the antibacterial activity of zinc oxide. *Int. J. Inorg. Mater.* **2001**, *3* (7), 643−646.
(32) Cheedarala, R. K.; Park, E.; Kong, K.; Park, Y.-B.; Park, H. W. Experimental study on critical heat flux of highly efficient soft hydrophilic CuO−chitosan nanofluid templates. *Int. J. Heat Mass Transfer* **2016**, *100*, 396−406.
(33) Baghayeri, M.; Veisi, H.; Farhadi, S.; Beitollahi, H.; Maleki, B. Ag nanoparticles decorated Fe3O4/chitosan nanocomposite: synthesis, characterization and application toward electrochemical sensing of hydrogen peroxide. *J. Iran. Chem. Soc.* **2018**, *15* (5), 1015−1022.
(34) Mujeeb Rahman, P.; Abdul Mujeeb, V. M.; Muraleedharan, K.; Thomas, S. K. Chitosan/nano ZnO composite films: Enhanced mechanical, antimicrobial and dielectric properties. *Arabian J. Chem.* **2018**, *11* (1), 120−127.
(35) Berthold, T.; Benstetter, G.; Frammelsberger, W.; Rodríguez, R.; Nafría, M. Nanoscale characterization of copper oxide films by Kelvin Probe Force Microscopy. *Thin Solid Films* **2015**, *584*, 310−315.
(36) Qin, H.; Wang, C. M.; Dong, Q. Q.; Zhang, L.; Zhang, X.; Ma, Z. Y.; Han, Q. R. Preparation and characterization of magnetic Fe3O4−chitosan nanoparticles loaded with isoniazid. *J. Magn. Magn. Mater.* **2015**, *381*, 120−126.
(37) Gaber Ahmed, G. H.; Fernández-González, A.; Díaz García, M. E. Nano-encapsulation of grape and apple pomace phenolic extract in chitosan and soy protein via nanoemulsification. *Food Hydrocolloids* **2020**, *108*, No. 105806.
(38) Liang, P.; Zhao, Y.; Shen, Q.; Wang, D.; Xu, D. The effect of carboxymethyl chitosan on the precipitation of calcium carbonate. *J. Cryst. Growth* **2004**, *261* (4), 571−576.
(39) Zhou, W.; He, W.; Zhong, S.; Wang, Y.; Zhao, H.; Li, Z.; Yan, S. Biosynthesis and magnetic properties of mesoporous Fe3O4 composites. *J. Magn. Magn. Mater.* **2009**, *321* (8), 1025−1028.
(40) Materón, E. M.; Miyazaki, C. M.; Carr, O.; Joshi, N.; Picciani, P. H. S.; Dalmaschio, C. J.; Davis, F.; Shimizu, F. M. Magnetic nanoparticles in biomedical applications: A review. *Appl. Surface Sci. Adv.* **2021**, *6*, No. 100163.
(41) Taufik, A.; Kalim, I.; Saleh, R. Preparation, Characterization and Photocatalytic Activity of Multifunctional Fe3O4/ZnO/CuO Hybrid Nanoparticles. *Mater. Sci. Forum* **2015**, *827*, 37−42.
(42) Zhang, L.-y.; Zhu, X.-j.; Sun, H.-w.; Chi, G.-r.; Xu, J.-x.; Sun, Y.-l. Control synthesis of magnetic Fe3O4−chitosan nanoparticles under UV irradiation in aqueous system. *Curr. Appl. Phys.* **2010**, *10* (3), 828−833.
(43) Seow, T. W.; Lim, C. K.*Removal of Dye by Adsorption: A Review*, 2016.
(44) Rizzi, V.; D'Agostino, F.; Fini, P.; Semeraro, P.; Cosma, P. An interesting environmental friendly cleanup: The excellent potential of olive pomace for disperse blue adsorption/desorption from wastewater. *Dyes Pigm.* **2017**, *140*, 480−490.
(45) Al-Ghouti, M. A.; Al-Absi, R. S. Mechanistic understanding of the adsorption and thermodynamic aspects of cationic methylene blue dye onto cellulosic olive stones biomass from wastewater. *Sci. Rep.* **2020**, *10* (1), No. 15928.
(46) Tsykhanovska, I.; Evlash, V.; Alexandrov, A.; Gontar, T. Dissolution kinetics of Fe3O4 Nanoparticles in the acid media. *Chem. Chem. Technol.* **2019**, *13* (2), 170−184.
(47) Tian, C.; Zhao, H.; Sun, H.; Xiao, K.; Keung Wong, P. Enhanced adsorption and photocatalytic activities of ultrathin graphitic carbon nitride nanosheets: Kinetics and mechanism. *Chem. Eng. J.* **2020**, *381*, No. 122760.
(48) Pham, T. M. H.; Nguyen, N. S.; Dao, T. N.; Le, T. T.; Nguyen, T. H.; Pham, H. N.; Nguyen, T. H. Facile Ultrasound-Assisted Green Synthesis of NiO/Chitosan Nanocomposite from Mangosteen Peel Extracts as Antibacterial Agents. *J. Nanomater.* **2022**, *2022*, No. 2485291.
(49) An, T. N. M.; Phuc, T. T.; Nhi, D. N. T.; Van Cuong, N. Removal of reactive red dye by reusable chitosan-polyaniline/Fe3O4 nanocomposite. *Vietnam J. Chem.* **2020**, *58* (4), 477−481.
(50) Maruthupandy, M.; Muneeswaran, T.; Anand, M.; Quero, F. Highly efficient multifunctional graphene/chitosan/magnetite nanocomposites for photocatalytic degradation of important dye molecules. *Int. J. Biol. Macromol.* **2020**, *153*, 736−746.
(51) Katowah, D. F.; Saleh, S. M.; Mohammed, G. I.; Alkayal, N. S.; Ali, R.; Hussein, M. A. Ultra-efficient hybrid material-based cross-linked PANI@Cs-GO-OXS/CuO for the photocatalytic degradation of Rhodamine-B. *J. Phys. Chem. Solids* **2021**, *157*, No. 110208.
(52) Motora, K. G.; Wu, C.-M. Magnetically separable highly efficient full-spectrum light-driven WO2.72/Fe3O4 nanocomposites for photocatalytic reduction of carcinogenic chromium (VI) and organic dye degradation. *J. Taiwan Inst. Chem. Eng.* **2020**, *117*, 123−132.
(53) Mousavi, M.; Habibi-Yangjeh, A.; Abitorabi, M. Fabrication of novel magnetically separable nanocomposites using graphitic carbon nitride, silver phosphate and silver chloride and their applications in photocatalytic removal of different pollutants using visible-light irradiation. *J. Colloid Interface Sci.* **2016**, *480*, 218−231.
(54) Warshagha, M. Z. A.; Muneer, M. Direct Z-Scheme AgBr/β-MnO2 Photocatalysts for Highly Efficient Photocatalytic and Anticancer Activity. *ACS Omega* **2022**, *7* (34), 30171−30183.
(55) Huang, X.; Zhou, H.; Yue, X.; Ran, S.; Zhu, J. Novel Magnetic Fe3O4/α-FeOOH Nanocomposites and Their Enhanced Mechanism for Tetracycline Hydrochloride Removal in the Visible Photo-Fenton Process. *ACS Omega* **2021**, *6* (13), 9095−9103.
(56) Pham, H. L.; Nguyen, V. D.; Nguyen, V. K.; Le, T. H. P.; Ta, N. B.; Pham, D. C.; Tran, Q. T.; Dang, V. T. Rational design of magnetically separable core/shell Fe3O4/ZnO heterostructures for enhanced visible-light photodegradation performance. *RSC Adv.* **2021**, *11* (36), 22317−22326.
(57) Rong, P.; Jiang, Y.-F.; Wang, Q.; Gu, M.; Jiang, X.-L.; Yu, Q. Photocatalytic degradation of methylene blue (MB) with Cu1−ZnO single atom catalysts on graphene-coated flexible substrates. *J. Mater. Chem. A* **2022**, *10* (11), 6231−6241.

https://doi.org/10.1021/acsomega.3c04956
ACS Omega 2023, 8, 42429−42439